CrossMark
click for updates

Structural and CO_2 capture analyses of the $Li_{1+x}FeO_2$ ($0 \leq x \leq 0.3$) system: effect of different physicochemical conditions

J. Francisco Gomez-Garcia* and Heriberto Pfeiffer

In this work, we studied α-$LiFeO_2$ compounds and the effect of lithium excess on CO_2 capture properties. The α-$LiFeO_2$ phase (cubic phase) was synthesized using the nitrate pyrolysis method at moderate temperature and a short calcination time (up to 670 °C and 3 h). Four compositions were synthesized with the nominal formula $Li_{1+x}FeO_2$ for $0 \leq x \leq 0.3$, obtaining α-$LiFeO_2$ phases with different lattice parameters. The specific surface area was calculated for all the compounds from the BET model, fitting the N_2 adsorption–desorption curves. The CO_2 capture was studied under two different sets of physicochemical conditions. Initially, the CO_2 capture was analysed at high temperature, where the $Li_{1.3}FeO_2$ composition showed the best properties at $T > 600$ °C. It was found that the amount of CO_2 captured at $T > 600$ °C depended on the lithium excess in the sample. Isothermal studies were performed in the 400–700 °C range, and the curves were fitted to a double exponential model. Kinetic constants were used in the Eyring formalism to obtain the activation enthalpies ($\Delta H^{\neq}$) for the surface and bulk reactions. These values were similar to those reported for other Li-based ceramics. The CO_2 capture process in the presence of steam was evaluated at low temperature (from 40 °C to 80 °C, varying the relative humidity from 0 to 80%). In these physicochemical conditions, $Li_{1.3}FeO_2$ could capture up to 24 wt% CO_2. This characterization has not previously been performed on these compounds. After CO_2 and steam capture, the product obtained contained magnetite, which is an iron oxide with mixed Fe^{2+} and Fe^{3+} oxidation states. The origin of the Fe^{2+} is attributed to the excess lithium added to the crystalline system. Its presence was confirmed by XPS spectroscopy, and it was also possible to identify two different chemical environments for oxygen ions, indicating that the Li^+ ions occupy two different crystal sites. We associated the high reactivity of compounds under a steam and CO_2 atmosphere with the presence of both Fe^{2+} and the interstitial Li^+ species.

Introduction

Over the past several years, the research community has focused on CO_2 capture technologies with a consequent increase in patents and research papers.[1] Most of the CO_2 capture technologies are based on cryogenic distillation,[2,3] oxyfuel systems,[4,5] fuel cell systems,[6] ionic liquids,[7,8] and adsorption[2–4,8,9] or sorption processes.[2,3,5] In the last case, solid sorbents have been widely studied in low, moderate and high temperatures,[9] showing that alkali metal ceramics have good capture capabilities in the moderate and high temperature ranges.[10]

Lithium- and sodium-based ceramics have shown interesting capture properties in their native oxide form,[11] as well as in zirconates,[12–15] silicates,[16–18] cuprates,[19] aluminates[20] and

titanates.[21,22] The capture properties have also been studied in low temperature conditions in the presence of steam.[23–25]

On the other hand, α-$LiFeO_2$ has a rock-salt type structure with a face-centred cubic arrangement of O^{2-} ions in which octahedral sites are randomly occupied by Fe^{3+} and Li^+ ions.[26] The other crystal phases reported for $LiFeO_2$ are the tetragonal, trigonal and orthorhombic phases labelled γ-$LiFeO_2$, β-$LiFeO_2$ and o-$LiFeO_2$, respectively.[26–29] The reagents and synthesis method play an important role in obtaining a particular crystal phase.[27] $LiFeO_2$ has also been studied as an electrolyte or a cathode for lithium batteries.[26,29] Lithium ferrites have been studied for CO_2 capture between 200 and 600 °C.[30–32] In these studies, the capture capability strongly depended on the amount of cubic phase in the sample,[30] achieving up to 16 wt% CO_2 uptake at 400 °C in a CO_2 flow after 2 h of exposure.[31,32] In dynamic conditions, up to 5 wt% of capture has been reported at the same temperature.[30] Nevertheless, the capture capability decreases rapidly above 500 °C; detailed experiments concerning the kinetics of capture or the influence of the lithium composition have not been reported until now.
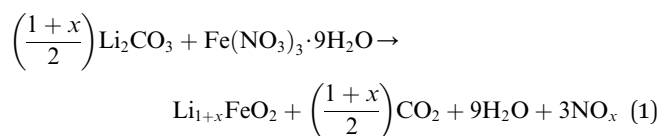
Instituto de Investigaciones en Materiales, Universidad Nacional Autónoma de México, Circuito Exterior s/n, CU, del. Coyoacán, CP 04510, Ciudad de México, Mexico. E-mail: jfrancisco@comunidad.unam.mx; Fax: +52 55 56161371; Tel: +52 55 56224627

In this context, the aim of the present work was to synthesize and characterize different $Li_{1+x}FeO_2$ ($0 \leq x \leq 0.3$) compositions using a novel method that employs low temperatures and short reaction times, followed by a structural and microstructural study of the effect of lithium excess on the CO_2 capture capability of each compound. Moreover, the effect of temperature and the effect of steam at low temperature on the CO_2 capture process using each of the compositions were studied.

Experimental section

Synthesis

Cubic lithium ferrite (α-$LiFeO_2$) was synthesized using the nitrate pyrolysis method. Stoichiometric amounts of lithium carbonate (Li_2CO_3, MEYER® (>99%) from México) and iron nitrate(III) nonahydrate ($Fe(NO_3)_3 \cdot 9H_2O$, MEYER® (>99%) from México) were dissolved and mixed together with distilled water, where nitric acid (HNO_3, 10 M, ACS reagent Sigma-Aldrich from México) was added, dropwise, until the Li_2CO_3 dissolved. The solution was dried, and the solid was calcined (in air with 0.16 atm of oxygen) at 500 °C for 3 h and then at 670 °C for 3 h, the second treatment ensuring a single phase in all the synthesized compounds. To evaluate the effects of lithium content in the α-$LiFeO_2$ lattice, different compounds with Li/Fe molar ratios of 1, 1.1, 1.2 and 1.3 were synthesized according to eqn (1), where x represents a lithium excess compared with the stoichiometric α-$LiFeO_2$.

$$\left(\frac{1+x}{2}\right)Li_2CO_3 + Fe(NO_3)_3 \cdot 9H_2O \rightarrow$$

$$Li_{1+x}FeO_2 + \left(\frac{1+x}{2}\right)CO_2 + 9H_2O + 3NO_x \quad (1)$$

Characterization

The compounds were labelled $x = 0$, 0.1, 0.2 and 0.3 according to the nominal formula $Li_{1+x}FeO_2$. The structural characterization was carried out by powder X-ray diffraction (XRD), using a D-5000 diffractometer (Siemens, from Germany) with a Co anode ($\lambda = 1.789$ Å). The phase was indexed as a cubic system and a further refinement by the Rietveld method was performed using GSAS[33] software with the EXPGUI interface.[34]

Electronic structure analyses were performed by X-ray photoelectron spectroscopy (XPS) in an ESCA2000 Multilab equipment (VG Microtech, from UK) with UHV system, Al K X-ray (1486.6 eV) and CLAM4 MCD analyser. The sample surface was sputtered for 10 minutes with 0.33 μA mm^{-2} Ar$^+$ ions produced at 4.5 kV. The peak positions on the XPS spectra were referenced to the C 1s core-level localized at 285.00 eV. The XPS spectra were deconvoluted using SDP v4.1 software. The curve fitting procedures for the signal analysis was as follows: (1) all spectra were calibrated to the C 1s peak at 285.00 eV as carbon is ubiquitous and present on any surface.[35] (2) The linear method for background subtraction was employed in the BE analysis range. (3) The Gaussian–Lorentzian ratio was fixed to 0.95 to simulate the peak profile. (4) The asymmetry factor was fixed to 0.2. (5) The peak positions for the Fe^{3+} $2p_{3/2}$ and Fe^{3+} $2p_{1/2}$ were

obtained from the first fit of the data for the $x = 0$ sample and then fixed for the following analyses. (6) The peak positions for the Fe^{2+} $2p_{3/2}$ and Fe^{2+} $2p_{1/2}$ were obtained from the work of McIntyre and Zetaruk,[36] and after further fitting, were fixed at 709.3 and 722.94 eV, respectively. (7) The full width at half maximum (FWHM) was initially determined on the $x = 0$ sample and was used as the initial parameter for the $x = 0.1$, 0.2 and 0.3 samples. (8) The best fit was selected by its minimum χ^2 value.

Surface area analysis was performed by N_2 adsorption–desorption curves at −196 °C in Minisorp II equipment (BEL-Japan, from Japan); the Brunauer–Emmett–Teller method (BET) was used to determine the specific surface area. CO_2 capture (dynamic and isothermal process) was measured in a Q500HR thermogravimetric balance (TA Instruments, from USA) with 60 mL min^{-1} gas flow from 40 °C to 800 °C. The CO_2 and steam capture was performed in a Q5000SA thermogravimetric balance (TA Instruments, from USA) at different values of temperature and relative humidity (RH). The experiments were carried out using N_2 and CO_2 gases. The total gas flow used in each experiment (dynamic and isothermal) was 100 mL min^{-1}. Further TGA and ATR-FTIR spectroscopy studies (Bruker Alpha-Platinum spectrometer from Germany) were performed for each product after CO_2–steam exposure.

Results and discussion

$Li_{1+x}FeO_2$ X-ray characterization

Four different $Li_{1+x}FeO_2$ compositions were synthesized by the novel process described above ($x = 0$, 0.1, 0.2 and 0.3). The colour of the powder samples varied depending on the lithium excess: the $x = 0$ and 0.1 compositions turned from orange to orange-brown, while the samples with $x = 0.2$ and 0.3 were black. All compositions showed a single-phase X-ray pattern (Fig. 1) and were indexed as a cubic crystal system. The reflection conditions show that the cubic unit cell is face-centred (FCC), matching the α-$LiFeO_2$ phase, which has a $Fm\bar{3}m$ space group (no. 225).[37] There were no other diffractions associated with the tetragonal $LiFeO_2$ polymorph or other crystal phases.

The experimental X-ray patterns were refined using the Rietveld method. As the α-$LiFeO_2$ phase is isostructural to rock-salt, only the lattice parameter and thermal factors were available to fit. The results of these refinements are summarized in Table 1. In addition, Fig. 2 shows the behaviour of the $Li_{1+x}FeO_2$ lattice parameter as a function of lithium content. A linear behaviour is observed at $x < 0.2$ values, indicating a solid solution system according to law of Vegard.[38] Between $x = 0.2$ and $x = 0.3$, the system does not behave as a Vegard solid solution. Thus, it may be supposed that the solubility limit is reached in this composition range. In fact, at $x > 0.3$ compositions, the samples displayed an X-ray pattern with two crystal phases (α-$LiFeO_2$ and Li_5FeO_4, data not shown). The square inset of Fig. 2 shows the α-$LiFeO_2$ unit cell. In the α-$LiFeO_2$ phase, oxygen ions are placed in an FCC arrangement with all octahedral holes occupied by Fe^{3+} or Li^+ (in a random distribution). This image also displays the tetrahedral holes made by the FCC lattice, in which excess lithium can be placed.
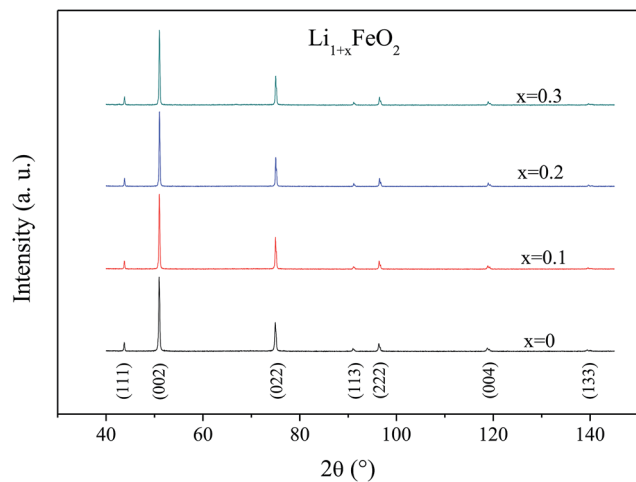
Fig. 1 X-ray patterns for $Li_{1+x}FeO_2$ system, where x varied between 0 and 0.3. All patterns were indexed as a cubic crystal system. The (hkl) for each reflection are in the bottom of the graph.

Table 1 Parameters obtained by Rietveld refinement on experimental X-ray patterns of $Li_{1+x}FeO_2$ system

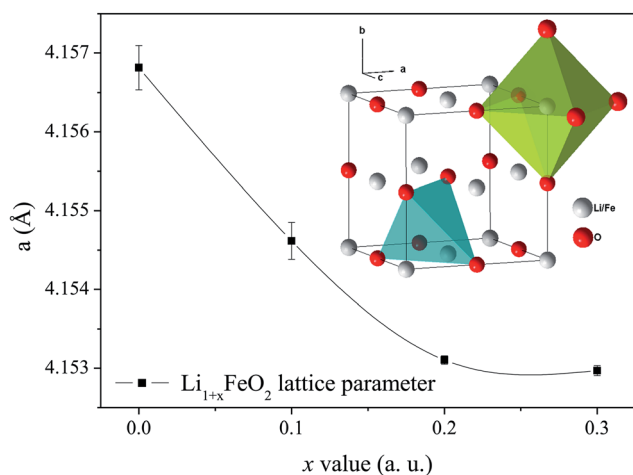| x value	a (Å)	R_{wp}	χ^2
0	4.1568(2)	0.0890	1.243
0.1	4.1546(2)	0.0856	1.240
0.2	4.15310(5)	0.0862	1.263
0.3	4.15297(6)	0.0886	1.169

Fig. 2 Lattice parameter as a function of lithium content. Inner in graph there is a unit cell for the α-$LiFeO_2$ phase with Fe^{3+} octahedra (green) and in blue are shown the tetrahedral holes formed by O^{2-}.

The N_2 adsorption–desorption isotherms at −196 °C for each of the $Li_{1+x}FeO_2$ compositions are presented in Fig. 3. All samples presented type II isotherms according to the IUPAC classification,[39] which is characteristic for a non-porous material. Moreover, the isotherm for the $x = 0.2$ sample presented

a narrow desorption hysteresis loop (type H4 according to IUPAC classification[39]), related with the presence of porosity in the sample, which was not relevant in the capture process. Finally, the BET model was employed to calculate the specific surface area. The areas were 4.8 m^2 g^{-1}, 1.2 m^2 g^{-1}, 2.3 m^2 g^{-1} and 1.0 m^2 g^{-1} for the $x = 0$, 0.1, 0.2 and 0.3 samples, respectively. A correlation between the specific surface area and the chemical composition of the samples was not observed. However, the $Li_{1+x}FeO_2$ composition without lithium excess ($x = 0$) had the highest surface area, which suggests that lithium excess tends to decrease the surface area. This result may be attributed to a faster sintering process produced by the high lithium mobility.

High temperature CO_2 capture

After the structural and microstructural characterization, all the $Li_{1+x}FeO_2$ compositions were analysed for CO_2 capture under different physicochemical conditions. Initially, CO_2 capture was dynamically evaluated from 40 °C to 800 °C (see Fig. 4). For the $x = 0$ sample (black squares in Fig. 4), a maximum CO_2 capture was observed (2 wt%) near 500 °C; above 550 °C, the capture decreased to 0 wt% (this feature implies that the $x = 0$ sample in not suitable for CO_2 capture at $T > 550$ °C). The CO_2 capture at 500 °C of $LiFeO_2$ has been described in previous research. Yanase and co-workers evaluated the CO_2 capture on α-$LiFeO_2$ after 2 h under CO_2 gas flow,[30] and they reported a plot with a similar profile as that depicted by the $x = 0$ compound. The authors assigned this behaviour to the high specific surface area in their samples; the decrease in CO_2 capture at higher temperatures was caused by the decomposition of lithium carbonate.[30,32] In the present case, the $x = 0$ compound has the highest specific surface area (4.8 m^2 g^{-1}) and the highest CO_2 capture near 500 °C (approximately 1.5 wt%), but the $x = 0.3$ compound has the lowest specific surface area (1.0 m^2 g^{-1}) and a very similar CO_2 capture near 500 °C (1.5 wt%). Based on these results, the surface area does not seem to be the only factor that affects the CO_2 capture capacity at 500 °C; the decrease in the CO_2 capture capacity at temperatures higher than 550 °C could be due to the weak interaction between CO_2 and the surface in this specific case.

At 500 °C, the $x = 0.1$, 0.2 and 0.3 samples captured less CO_2 than the sample without lithium excess ($x = 0$). This may be related to the lower surface area of the $x = 0.1$, 0.2 and 0.3 samples. Nevertheless, the CO_2 capture behaviour changed at higher temperatures ($T > 600$ °C). While the $x = 0$ sample totally desorbed CO_2 at $T > 600$ °C, all other samples presented a second weight change after a superficial CO_2 chemisorption–desorption equilibrium. In fact, at the maximum temperature (800 °C), the final weight changes were 1.1, 2.4 and 4.4 wt% for x values of 0.1, 0.2 and 0.3, respectively. It seems that the lithium excess can diffuse and react with CO_2 in this temperature range.

The $Li_{1+x}FeO_2$ sample with $x = 0.3$ showed the highest CO_2 capture capacity in the dynamic thermograms. Therefore, its capture properties were isothermally evaluated from 400 °C to 700 °C at each 50 °C increment. The results of these experiments are shown in Fig. 5 (left side), where it is possible to
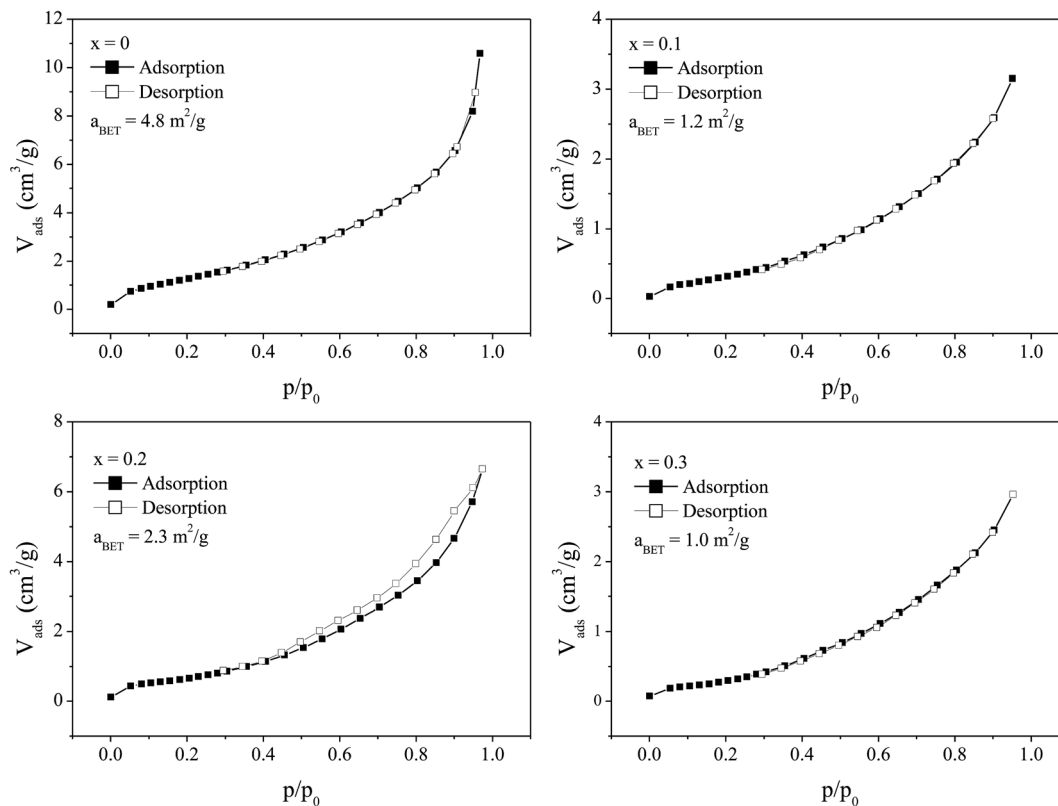
Fig. 3 N_2 adsorption–desorption curves for samples studied in this work. Filled symbols show the adsorption curve and empty symbols display the desorption curve.
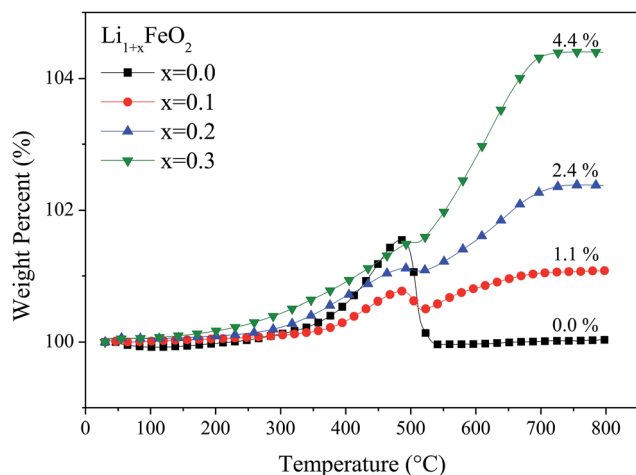

Fig. 4 Dynamic TG curves of the CO_2 capture for $Li_{1+x}FeO_2$ system. At $T > 600$ °C the system captures CO_2 according to the lithium excess.

observe that CO_2 capture between 400 °C and 650 °C increases with increasing temperature. After 180 minutes, the final weight gains for each experiment were 2.7, 3.1, 3.8, 3.7, 4.0 and 4.0 wt% as a function of temperature. The last two values correspond to the 600 °C and 650 °C experiments, respectively, and the mass gain for those experiments is similar to that showed in the dynamic experiment (4.4%). The CO_2 capture rate was affected by the temperature, as the profiles become steeper at higher

temperature in Fig. 5. The isotherm performed at 700 °C presents the steepest profile, implying the greatest capture rate, although this isotherm also presented the lowest mass gain (2.4 wt%). This might be due to a sintering process that blocks the CO_2 diffusion in the sample.

The products of isothermal CO_2 capture were characterized by ATR-FTIR spectroscopy (Fig. 5 right side), where the main signals were found to correspond to lithium carbonate, confirming the sample carbonation.

According to the literature, this type of isothermal experiment is usually fit to a double exponential equation[13,40] that represents two capture processes that occur at different rates (k_1 and k_2). Usually, $k_1 \gg k_2$, and these kinetic constants are associated with the CO_2 capture at the superficial level and the CO_2 capture in the particle bulk. Each process is available to capture a defined quantity of CO_2 represented by constants A and B, and C is the total amount captured in the compound ($C = A + B$).

$$y = -A \exp(-k_1 t) - B \exp(-k_2 t) + C \qquad (2)$$

Each $Li_{1.3}FeO_2$–CO_2 isotherm was fit to eqn (2), and the rate and pre-exponential constants were obtained from this calculation. The corresponding CO_2 capture activation enthalpies ($\Delta H^{\neq}$) were calculated using the Eyring model.[40] The Eyring formulation is presented in eqn (3), where R is the ideal gas constant, k_B is the Boltzmann constant, h is the Planck constant and $\Delta S^{\neq}$ is the entropy associated with the capture process.
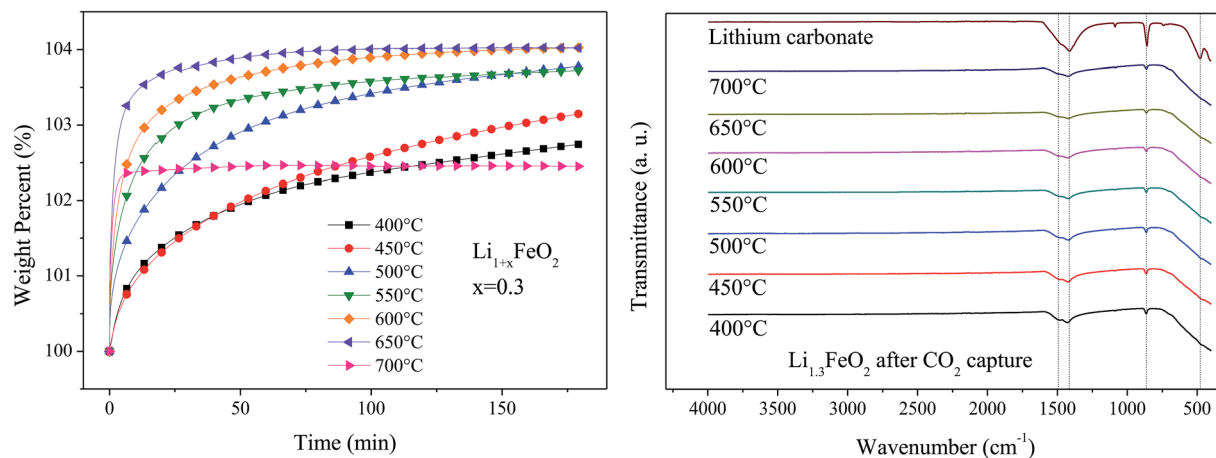
Fig. 5 Isothermal thermogravimetric experiments performed on $Li_{1+x}FeO_2$ with $x = 0.3$ (Left). ATR-FTIR spectra for each product of the corresponding isothermal experiment (Right).

$$\ln\left(\frac{k}{T}\right) = -\left(\frac{\Delta H^{\neq}}{R}\right)\left(\frac{1}{T}\right) + \ln\left(\frac{k_B}{h}\right) + \frac{\Delta S^{\neq}}{R} \qquad (3)$$

Fig. 6 shows the linear plots derived from the Eyring model, where it is possible to see that both processes (superficial and bulk capture) present linear behaviour between 450 °C and 700 °C. The enthalpies calculated within this region were 36.1 and 33.6 kJ mol^{-1} for the superficial and bulk CO_2 capture processes, respectively. These values are similar to those obtained for other alkali ceramics, such as the Li_4SiO_4–CO_2 system with 37.2 kJ mol^{-1},[40] Na_2ZrO_3 with 36.68 kJ mol^{-1} (ref. 13) or Li_5AlO_4 with 15.66 kJ mol^{-1} (ref. 20) for the superficial CO_2 capture process.

Considering that samples containing lithium excess have higher CO_2 captures, one could conclude that only the excess lithium is responsible for the CO_2 capture capacity. In this scenario, the reaction between $Li_{1+x}FeO_2$ and CO_2 is represented

by eqn (4), where lithium carbonate formation should produce an oxygen-deficient $LiFeO_2$ compound.

$$Li_{1+x}FeO_2 + CO_2 \xrightarrow{T > 600\ °C} LiFeO_{2-\frac{x}{2}} + \frac{x}{2}Li_2CO_3 \qquad (4)$$
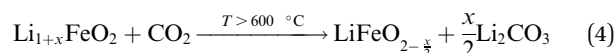
Under this hypothesis, the theoretical CO_2 capture of the $x = 0.3$ compound could be 6.8 wt%, but experimentally, the sample captured approximately 4 wt%. This means that a portion of the excess lithium does not react with CO_2. Thus, excess lithium ions may occupy two different crystallographic sites in the α-$LiFeO_2$ phase, as represented in eqn (5) with Kröger–Vink notation, where half of the excess lithium ions occupy interstitial sites, producing Fe^{2+} in the lattice. The existence of the Fe^{2+} is supported by the observations that the samples become darker in colour with increasing Li excess and that only the interstitial lithium is available to react with CO_2. Therefore, these compounds will be able to capture only half of the ideal weight described in eqn (4), i.e., 3.4%, which is similar to the 4% observed experimentally for the $x = 0.3$ sample. The fact that the $LiFeO_2$ compound ($x = 0$) does not capture CO_2 at $T > 600$ °C indicates that the lithium ions located in octahedral positions do not react with CO_2. According to eqn (5), the interstitial lithium should occupy the empty tetrahedral positions in the FCC lattice of α-$LiFeO_2$ phase, which indicates a different reactivity in a CO_2 atmosphere.

$$Li_2O \xrightarrow{LiFeO_2} Li_{Li}^{\times} + Li_i^{\bullet} + O_O^{\times} + Fe_{Fe}' \qquad (5)$$
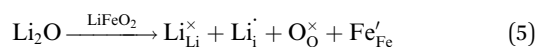
XPS characterization

To corroborate the presence of Fe^{2+} in $Li_{1+x}FeO_2$, XPS analysis was performed, which has been used to identify Fe^{2+} in various oxide materials.[35,36,41] Although XPS spectroscopy can measure the chemical composition, in the case of $LiFeO_2$, the peak due to the Li 2s binding energy (BE) is near 55 eV,[42] which overlaps with the Fe 3p BE peak (near to 56 eV). This fact makes XPS unsuitable for measuring the Li–Fe chemical composition.
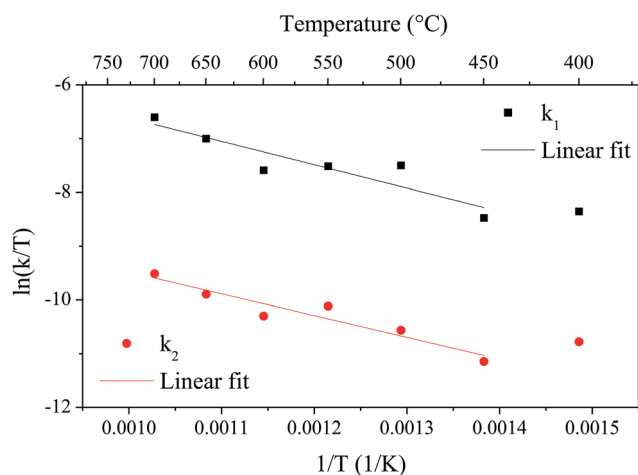

Fig. 6 Linear plots for Eyring model. Single symbols are the fitted kinetic constants from the double exponential model, while lines are the corresponding linear fitting according Eyring equation.

There are no interferences for the signals associated with the Fe 2p and the O 1s BE. Therefore, these signals can be studied to understand the chemical environment around the Fe and O ions.

Fig. 7 shows the deconvoluted Fe 2p XPS spectra for the $x = 0$ and $x = 0.3$ samples. Both spectra display the characteristic Fe^{3+} $2p_{3/2}$ and Fe^{3+} $2p_{1/2}$ peaks at 710.51 and 724.15 eV, respectively, with their associated satellite peaks at 718.21 and 732.09 eV, respectively, which are situated at 8 eV higher as in other iron oxides.[35] Peaks associated with the Fe^{2+} $2p_{3/2}$ and Fe^{2+} $2p_{1/2}$ can also be found in each XPS spectrum. The molar percent of Fe^{2+} present in the samples varied from 1% to 6.2%. Therefore, the amount of Fe^{2+} detected by XPS increased with increasing lithium content. The results for each deconvoluted Fe 2p XPS spectrum and the Fe^{2+} composition are summarized in Table 2.

Fig. 8 presents the deconvoluted XPS spectra of the O 1s peak for the $x = 0$ and 0.3 samples. All compounds present a prominent peak at 529.40 eV, which can be associated with the O 1s BE. This value is in agreement with the previously reported O 1s BE of various iron oxides, which are near 530 eV.[43] In the $x = 0$ sample (Fig. 8 left), there is a peak located at 530.48 eV, which

can be assigned to hydroxyl species or C–O bonds[36] that are situated at higher energy due to their covalent character. This peak vanishes as the lithium content increases. For the lithium excess samples, another peak appeared at 531.68 eV (Fig. 8 right), which indicates that there are two different chemical environments for the O^{2-} ion. The intensity of the peak situated at 531.68 eV increases with increasing lithium content. In eqn (5), lithium in a tetrahedral site was proposed as an interstitial defect in the lattice. The presence of lithium on tetrahedral sites must modify the BE for the Li and O levels. Because it is not possible to distinguish the BE for lithium in these compounds due to the overlap with the Fe 3p BE only the changes in the oxygen BE can be observed. Therefore, the peak at 531.68 eV could be the result of the presence of interstitial lithium. In the literature, it is known that the O 1s BE is 531.9 eV in Li_2O.[42] In that lattice, the lithium is surrounded by four oxygen ions (tetrahedral coordination), which is similar to the coordination of the interstitial lithium in the studied compounds (see Fig. 2). Therefore, the O 1s peak at 529.40 eV corresponds to the octahedral O–(Fe,Li) coordination, and the O 1s peak at 531.68 eV corresponds to the tetrahedral O–Li
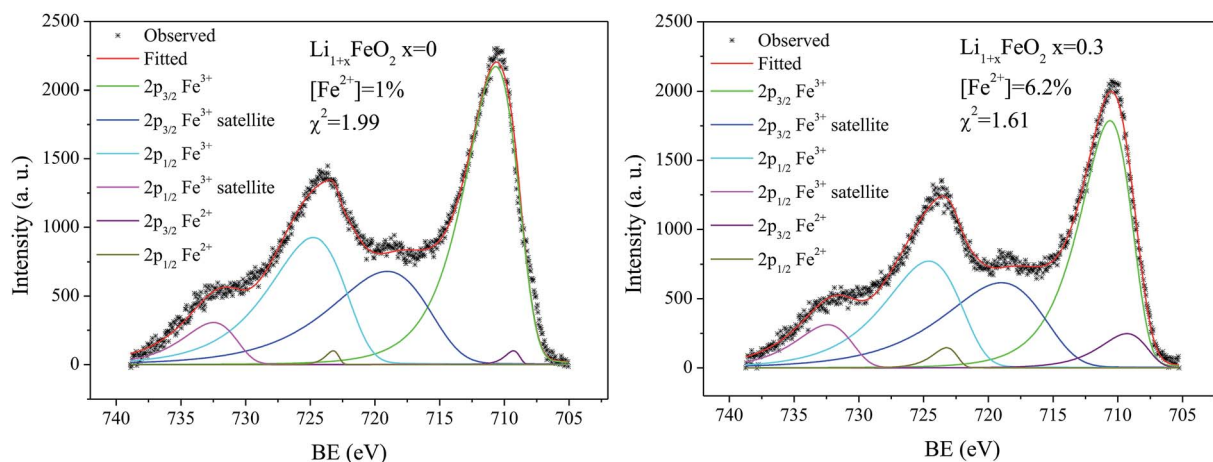

Fig. 7 XPS spectra of the Fe 2p for the $x = 0$ sample (left) and $x = 0.3$ sample (right). In both spectra there are Fe^{2+} signals which rises with the lithium excess in each samples.

Table 2 Peak positions for the XPS Fe 2p and O 1s peaks. The table also presents the percent of Fe^{2+} and the percent of oxygen in octahedral on tetrahedral coordination

| Sample | Peak position (eV) | | | | | | Fe^{2+} (%) | χ^2 | O 1s peak | | | | |
| | Main peak | | | | Satellite | | | | Octahedral | | Tetrahedral | | |
| | Fe^{3+} | | Fe^{2+} | | Fe^{3+} | | | | | | | | |
	$2p_{3/2}$	$2p_{1/2}$	$2p_{3/2}$	$2p_{1/2}$	$2p_{3/2}$	$2p_{1/2}$			Position (eV)	Ratio (%)	Position (eV)	Ratio (%)	χ^2
$x = 0$	710.67	724.77	709.30	723.23	719.06	732.48	1.0	1.98	529.40	90.2	531.58	9.8	1.57
$x = 0.1$	710.61	724.60	709.30	723.23	718.99	732.40	3.1	1.99	529.40	80.7	531.58	19.2	2.33
$x = 0.2$	710.61	724.60	709.30	723.23	718.99	732.40	5.7	1.57	529.40	78.3	531.62	21.7	2.72
$x = 0.3$	710.61	724.60	709.30	723.23	718.99	732.40	6.2	1.61	529.40	66.3	531.62	33.7	2.09
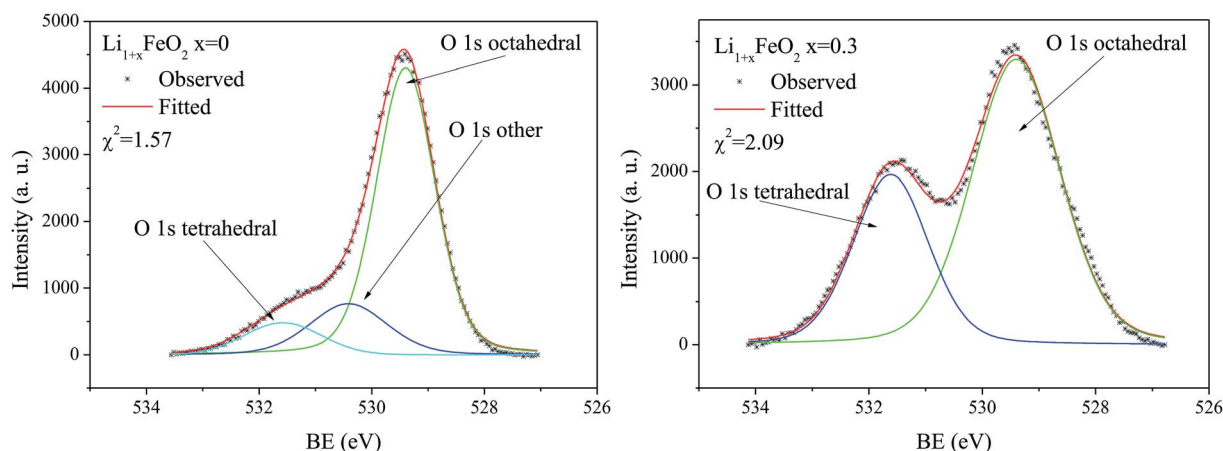
Fig. 8 Deconvoluted O 1s XPS spectra for $x = 0$ sample (left) and for $x = 0.3$ sample (right). The samples present two different chemical environment for oxygen ions, the peak at 529.40 eV is associated to O−(Fe,Li) in an octahedral disposition. The peak at 531.68 eV is associated to O−Li in a tetrahedral coordination.

coordination. The octahedral and tetrahedral oxygen ratio is presented in Table 2.

Effect of steam on CO_2 capture at low temperatures

It has been reported that in some cases steam enhances the CO_2 capture capacity at low temperatures.[44–46] For this reason, the effect of steam on CO_2 capture in the $Li_{1+x}FeO_2$ system was studied. In Fig. 9 (left side), the adsorption–desorption curves in a CO_2 and steam atmosphere are shown. The mass captured by the compounds increases as a function of the lithium content, although the $x = 0.2$ and $x = 0.3$ samples have very similar weight percentage changes. The amount of CO_2 captured is larger than that observed for the compositions in the absence of steam. To corroborate the steam effect in the CO_2 capture, a parallel experiment was performed using N_2 as the carrier gas (Fig. 9 right). In this figure, the combined effects CO_2 and steam produced a total weight change of 10.9 wt%, while the experiment in the presence of N_2 only gained 0.7 wt%. Therefore, the

high weight changes observed in the samples are a synergistic effect produced by CO_2 and steam.

The kinetics of CO_2 capture were evaluated by varying the lithium content in $Li_{1+x}FeO_2$ (Fig. 10 left side) at a fixed relative humidity (80%) and temperature (60 °C). The total weight changes during the CO_2 and steam sorption processes increased as a function of the lithium excess. The $x = 0$ sample has a 0.7 wt% change associated with water sorption only. The $x = 0.1$, 0.2 and 0.3 compounds achieved 2.2 wt%, 5.4 wt% and 9.2 wt% increases, respectively. The isotherms of the $x = 0.1$, 0.2 and 0.3 samples indicate that equilibrium was not reached after 180 minutes. The kinetic properties of CO_2 capture on the $x = 0.3$ sample were evaluated at different temperatures at a constant RH of 80% (Fig. 10 right side). As the temperature increases, the weight capture changes from 5.6 wt% at 40 °C to 23.6 wt% at 80 °C, which is more than the theoretical CO_2 capture capacity (22.3 wt% for $LiFeO_2$). In this experiment, even after 180 minutes of capture, the sample had not reached its capture capacity.
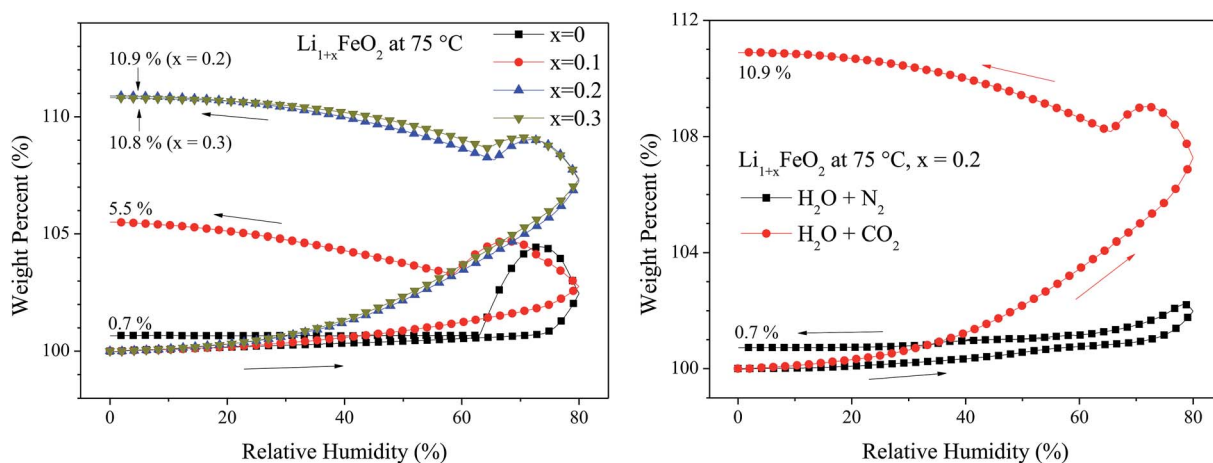

Fig. 9 Sorption and desorption curves of CO_2/N_2 and relative humidity. CO_2 atmosphere for all compounds studied (Left). Sorption difference between in CO_2−water steam atmosphere and inert gas (N_2) − water steam atmosphere for $Li_{1+x}FeO_2$ with $x = 0.2$ (Right).
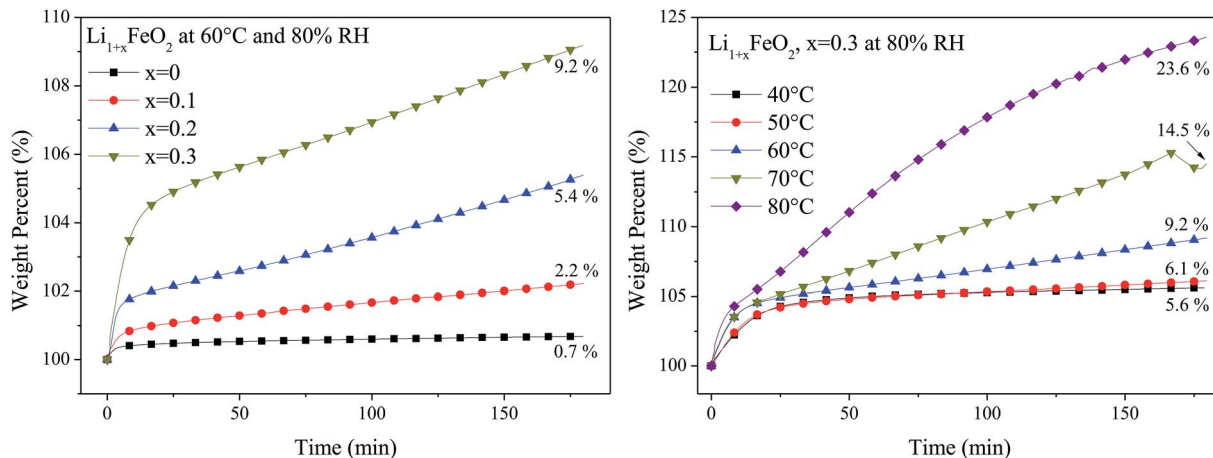
Fig. 10 Isothermal thermogravimetric studies at 80% of relative humidity. At 60 °C for all compounds studied (Left). At several temperatures for $Li_{1+x}FeO_2$ with $x = 0.3$ (Right).

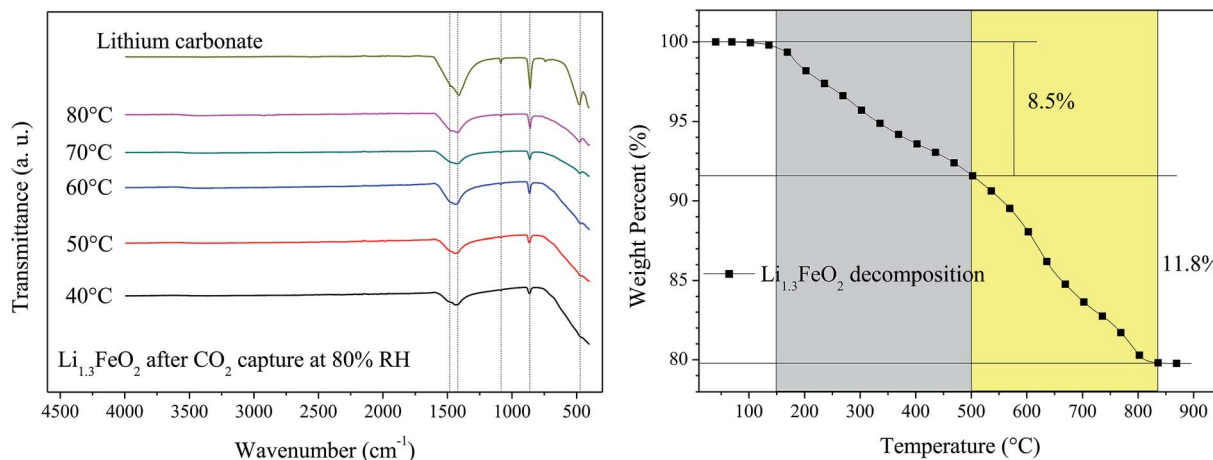**Fig. 11** Characterization of compounds after CO_2 and water steam adsorption of $Li_{1+x}FeO_2$ with $x = 0.3$. ATR-FTIR spectra for the different temperatures (Left). Thermogravimetric decomposition of the capture experiment at 80 °C and 80% of relative humidity (Right).

ATR-FTIR spectroscopy was employed to analyse the products for the $x = 0.3$ sample following capture at different temperatures, 80% RH and 180 minutes of treatment. Fig. 11 (left side) shows the presence of signals characteristic of lithium carbonate but no signals characteristic of H_2O or O–H species (e.g., lithium hydroxide). Fig. 11 (right side) displays the thermogravimetric decomposition of the $x = 0.3$ sample showing that the mass loss below 150 °C is less than 1 wt%. This corroborates that steam is poorly adsorbed in the samples. However, in the interval of 150 °C to 500 °C the mass loss is nearly 8.5 wt%. This could be due to the decarbonation process in which the CO_2 is weakly bonded to the sample. At $T > 500$ °C bulk decarbonation occurs. In this temperature range, the weight lost is nearly 11.8 wt%. The total weight loss was 20 wt%, which is equivalent to 23 wt% capture in the $x = 0.3$ sample at 80 °C and 80% RH.

An X-ray pattern was obtained for the isothermal product obtained following CO_2 capture at 80 °C and 80% relative humidity (Fig. 12). The reflections presented in this XRD
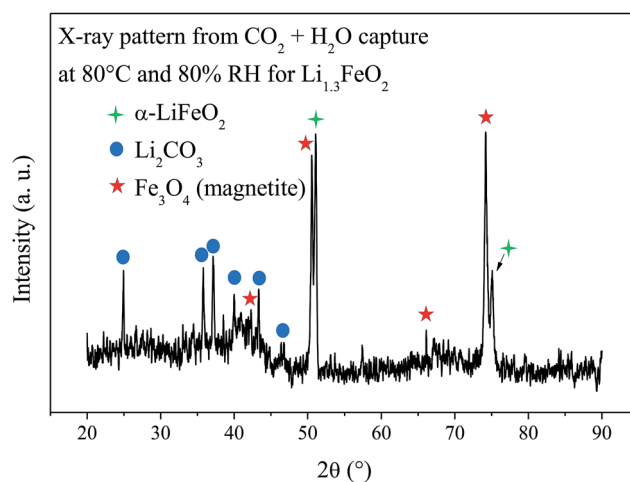

Fig. 12 X-ray pattern after the CO_2 and water steam sorption on $Li_{1+x}FeO_2$ with $x = 0.3$ at 80 °C and 80% of relative humidity.

pattern were identified as Li_2CO_3 (JCPDS no. 99-101-1959), cubic $LiFeO_2$ (JCPDS no. 01-074-2284) and Fe_3O_4 (magnetite JCPDS no. 99-100-6943). Reflections associated with LiOH or $LiOH \cdot H_2O$ were not found. It is remarkable that the magnetite phase appears in this experiment because the oxygen deficient phase of ferrous oxide appeared. The presence of magnetite phase in the CO_2–steam capture product is consistent with the magnetization displayed by the powder against steel labware. Lithium hydroxide was not observable by X-ray or by ATR-FTIR. Thus, it may be concluded that only Li_2CO_3 is responsible for the weight loss in the thermogravimetric analysis (Fig. 9).

Moreover, the presence of magnetite as a product of CO_2 and steam capture for the $x = 0.3$ sample is indicative of the presence of Fe^{2+} in the $Li_{1.3}FeO_2$ lattice. At the experimental conditions, a redox reaction would not be possible, so the Fe^{2+} must be formed during the synthesis process; then, in the capture experiment, the steam and CO_2 react with the $Li_{1.3}FeO_2$ to form magnetite (Fe_3O_4 with an Fe^{3+}/Fe^{2+} molar ratio of 2). These results imply that if a significant amount of the Fe^{3+} present in the $Li_{1.3}FeO_2$ is removed from the ferrite lattice to form magnetite, then lithium oxide is available to react with CO_2 to form lithium carbonate. Therefore, the amount of Fe^{2+} ions is the limiting reagent in the capture process, as shown in Fig. 10, where the weight changes are proportional to the lithium excess. Additionally, it is evident from the same figure that the $x = 0$ compound has a CO_2 capture of approximately 1 wt% after 180 minutes. A similar weight change was produced by the $x = 0.2$ compound in Fig. 9 (right side) when the atmosphere was N_2 and steam. Therefore, it is possible that the $LiFeO_2$ compound does not react in the CO_2 and steam atmosphere but only absorbs water.

Conclusions

The α-$LiFeO_2$ phase was synthesized by a novel method of nitrate pyrolysis involving two calcinations at 500 and 670 °C for 3 h. The synthesis was performed with Li/Fe molar ratios of 1, 1.1, 1.2 and 1.3. All compositions displayed the same crystal phase and a linear increase in its lattice parameters with increasing Li/Fe ratio, suggesting the formation of solid solutions with the nominal formula $Li_{1+x}FeO_2$ at $0 \leq x \leq 0.3$. The BET analyses on nitrogen adsorption–desorption curves at -196 °C show a specific surface area in the range of 1–4 m^2 g^{-1}. The amount of CO_2 captured increased with increasing lithium excess in the compound, and the $x = 0.3$ composition captured 4 wt% of CO_2 at $T > 600$ °C. The CO_2 capture capacity was related to the excess lithium in each sample, which can be placed at the interstitial positions on the FCC lattice. The isothermal thermogravimetric analyses in the 400 °C to 700 °C range were fit to the double exponential model, and the kinetic constants were evaluated using the Eyring model. The estimated $\Delta H^{\neq}$ for superficial and bulk capture were 36.1 and 33.6 kJ mol^{-1}, respectively. These values are close to those reported for other Li-based ceramics. The CO_2 capture capacity increased at lower temperatures in a steam atmosphere, with a 23.6 wt% weight change at 80 °C and 80% of relative humidity for the $x = 0.3$ compound. The ATR-FTIR spectra of all products following CO_2 capture showed only the signals corresponding to lithium carbonate. Therefore, the 23.6 wt% mass gain is due to CO_2 capture only. The $x = 0.3$ sample after CO_2 capture at 80 °C and 80% relative humidity contained the crystal phases of lithium carbonate, α-$LiFeO_2$ and Fe_3O_4 (magnetite) by XRD analysis. Therefore, we propose that part of the lithium excess is located as an interstitial defect and that it forms Fe^{2+} as a charge compensating defect. The presence of Fe^{2+} ions induces the magnetite formation during reaction with CO_2, which removes two Fe^{3+} cations from the $LiFeO_2$ structure for each Fe^{2+} ion removed, leading to a significant amount of LiO_2 free to react with CO_2. We discovered that the greater the lithium excess in the compound is, the greater the Fe^{2+} content is, and consequently, the greater the CO_2 capture in a steam atmosphere is. This was corroborated by finding two peaks in the XPS analysis of the O 1s BE, which indicates two different chemical environments associated with two different crystal sites for Li^+: one in octahedral coordination, which is a regular lattice site in the $LiFeO_2$ structure, and the other in tetrahedral coordination, which implies an interstitial defect. The Fe^{2+} content, as measured with XPS analysis of the Fe 2p BE, increased with increasing lithium excess. This result supports our hypothesis: the interstitial lithium ions in the $LiFeO_2$ structure modify the system reactivity in the presence of a steam and CO_2 atmosphere, resulting in a material with an enhanced CO_2 capture capability (up to 23.6 wt%) at lower temperature (80 °C) compared to a dry CO_2 atmosphere with a CO_2 capture capability up to 4.4 wt% at $T > 600$ °C.

Acknowledgements

References

1 B. Li, Y. Duan, D. Luebke and B. Morreale, *Appl. Energy*, 2013, **102**, 1439–1447.

2 B. P. Spigarelli and S. K. Kawatra, *J. CO2 Util.*, 2013, **1**, 69–87.

3 J. C. M. Pires, F. G. Martins, M. C. M. Alvim-Ferraz and M. Simões, *Chem. Eng. Res. Des.*, 2011, **89**, 1446–1460.

4 N. MacDowell, N. Florin, A. Buchard, J. Hallett, A. Galindo, G. Jackson, C. S. Adjiman, C. K. Williams, N. Shah and P. Fennell, *Energy Environ. Sci.*, 2010, **3**, 1645.

5 M. E. Boot-Handford, J. C. Abanades, E. J. Anthony, M. J. Blunt, S. Brandani, N. Mac Dowell, J. R. Fernández, M.-C. Ferrari, R. Gross, J. P. Hallett, R. S. Haszeldine, P. Heptonstall, A. Lyngfelt, Z. Makuch, E. Mangano, R. T. J. Porter, M. Pourkashanian, G. T. Rochelle, N. Shah, J. G. Yao and P. S. Fennell, *Energy Environ. Sci.*, 2014, **7**, 130–189.

6 J.-H. Wee, *Renewable Sustainable Energy Rev.*, 2014, **32**, 178–191.

7 X. Zhang, X. Zhang, H. Dong, Z. Zhao, S. Zhang and Y. Huang, *Energy Environ. Sci.*, 2012, **5**, 6668.

8 C.-H. Yu, *Aerosol Air Qual. Res.*, 2012, 745–769.

9 Q. Wang, J. Luo, Z. Zhong and A. Borgna, *Energy Environ. Sci.*, 2011, **4**, 42–55.

10 S. Kumar and S. K. Saxena, *Mater. Renew. Sustain. Energy*, 2014, **3**, 30.

11 H. A. Mosqueda, C. Vazquez, P. Bosch and H. Pfeiffer, *Chem. Mater.*, 2006, **18**, 2307–2310.

12 H. Pfeiffer and P. Bosch, *Chem. Mater.*, 2005, **17**, 1704–1710.

13 I. Alcérreca-Corte, E. Fregoso-Israel and H. Pfeiffer, *J. Phys. Chem. C*, 2008, **112**, 6520–6525.

14 E. Ochoa-Fernández, M. Rønning, T. Grande and D. Chen, *Chem. Mater.*, 2006, **18**, 6037–6046.

15 Y. Duan and J. Lekse, *Phys. Chem. Chem. Phys.*, 2015, **17**, 22543–22547.

16 M. T. Rodríguez and H. Pfeiffer, *Thermochim. Acta*, 2008, **473**, 92–95.

17 M. Mizunuma, M. Tsuda, Y. Maruo and T. Nakagaki, *Energy Procedia*, 2013, **37**, 1194–1201.

18 A. Sanna and M. M. Maroto-Valer, *Ind. Eng. Chem. Res.*, 2016, **55**, 4080–4088.

19 L. M. Palacios-Romero, E. Lima and H. Pfeiffer, *J. Phys. Chem. A*, 2009, **113**, 193–198.

20 T. Ávalos-Rendón, J. Casa-Madrid and H. Pfeiffer, *J. Phys. Chem. A*, 2009, **113**, 6919–6923.

21 P. Sánchez-Camacho, I. C. Romero-Ibarra, Y. Duan and H. Pfeiffer, *J. Phys. Chem. C*, 2014, **118**, 19822–19832.

22 A. López-Ortiz, N. G. P. Rivera, A. R. Rojas and D. L. Gutierrez, *Sep. Sci. Technol.*, 2005, **39**, 3559–3572.

23 L. Martínez-dlCruz and H. Pfeiffer, *J. Phys. Chem. C*, 2010, **114**, 9453–9458.

24 J. Ortiz-Landeros, L. Martínez-dlCruz, C. Gómez-Yáñez and H. Pfeiffer, *Thermochim. Acta*, 2011, **515**, 73–78.

25 R. Rodríguez-Mosqueda and H. Pfeiffer, *J. Phys. Chem. C*, 2013, **117**, 13452–13461.

26 A. E. Abdel-Ghany, A. Mauger, H. Groult, K. Zaghib and C. M. Julien, *J. Power Sources*, 2012, **197**, 285–291.

27 M. Tabuchi, *Solid State Ionics*, 1995, **79**, 220–226.

28 T. Shirane, *Solid State Ionics*, 1995, **79**, 227–233.

29 A. R. Armstrong, D. W. Tee, F. La Mantia, P. Novák and P. G. Bruce, *J. Am. Chem. Soc.*, 2008, **130**, 3554–3559.

30 I. Yanase, A. Kameyama and H. Kobayashi, *J. Ceram. Soc. Jpn.*, 2010, **118**, 48–51.

31 H. Eba and K. Sakurai, *Mater. Trans.*, 2005, **46**, 665–668.

32 I. Yanase, H. Otzuka and H. Kobayashi, *J. Ceram. Soc. Jpn.*, 2011, **119**, 933–938.

33 A. C. Larson and R. B. Von Dreele, *General Structure Analysis System (GSAS)*, Los Alamos National Laboratory Report LAUR, 1994, pp. 86–748.

34 B. H. Toby, *J. Appl. Crystallogr.*, 2001, **34**, 210–213.

35 T. Yamashita and P. Hayes, *Appl. Surf. Sci.*, 2008, **254**, 2441–2449.

36 N. S. McIntyre and D. G. Zetaruk, *Anal. Chem.*, 1977, **49**, 1521–1529.

37 J. C. Anderson and M. Schieber, *J. Phys. Chem. Solids*, 1964, **25**, 961–968.

38 L. Vegard, *Zeitschrift für Physik*, 1921, **5**, 17–26.

39 K. S. W. Sing, *Pure Appl. Chem.*, 1985, **57**, 603–619.

40 R. Rodríguez-Mosqueda and H. Pfeiffer, *J. Phys. Chem. A*, 2010, **114**, 4535–4541.

41 A. P. Grosvenor, B. A. Kobe, M. C. Biesinger and N. S. McIntyre, *Surf. Interface Anal.*, 2004, **36**, 1564–1574.

42 C. F. Mallinson, J. E. Castle and J. F. Watts, *Surf. Sci. Spectra*, 2013, **20**, 113–127.

43 T. Fujii, F. M. F. de Groot, G. A. Sawatzky, F. C. Voogt, T. Hibma and K. Okada, *Phys. Rev. B: Condens. Matter Mater. Phys.*, 1999, **59**, 3195–3202.

44 H. A. Lara-García, B. Alcántar-Vázquez, Y. Duan and H. Pfeiffer, *RSC Adv.*, 2015, **5**, 34157–34165.

45 S. Zhang, Q. Zhang, H. Wang, Y. Ni and Z. Zhu, *Int. J. Hydrogen Energy*, 2014, **39**, 17913–17920.

46 J. Fagerlund, J. Highfield and R. Zevenhoven, *RSC Adv.*, 2012, **2**, 10380.